



Effects of inclusion size and stress ratio on the very-high-cycle fatigue behavior of pearlitic steel

Tao Cong^{a,b}, Guian Qian^c, Guanzhen Zhang^b, Si Wu^b, Xiangnan Pan^c, Leiming Du^d, Xiaolong Liu^{a,*}

^a School of Mechanical Electronic & Control Engineering, Beijing Jiaotong University, Beijing 100044, China

^b Metals & Chemistry Research Institute, China Academy of Railway Sciences Corporation Limited, Beijing 100081, China

^c LNM, Institute of Mechanics, Chinese Academy of Sciences, Beijing 100190, China

^d School of Science, Harbin Institute of Technology, Shenzhen 518055, China

ARTICLE INFO

Keywords:

Pearlitic steel
Very-high-cycle fatigue
Inclusion size
Stress ratio
Nanograins

ABSTRACT

The effects of inclusion size and stress ratio (R) on the very-high-cycle fatigue (VHCF) behavior of pearlitic steel were experimentally assessed. The $S-N$ curve under rotating bending loading exhibited a horizontal asymptote shape and a clear fatigue limit. In contrast, the $S-N$ curve under ultrasonic axial loading exhibited a continuously descending shape, and the fatigue limit disappeared at a fatigue life of 10^7 cycles. The fine granular area (FGA) within nanograins formed in the crack initiation region only for the samples subjected to VHCF at $R = -1$. All instances of interior crack initiation were caused by the MnS inclusions.

1. Introduction

Shattered rims are typical failure mode of railway wheels, which will cause abrupt wheel fractures, rail damage, or even derailment in rare cases [1–3]. Fig. 1 shows the typical fracture surface morphology of a shattered rim, wherein the cracks initiated from the interior inclusion after being subjected to more than 10^7 cycles; hence, this phenomenon is considered a form of very-high-cycle fatigue (VHCF) in engineering applications [4,5]. With the situation that VHCF of railway wheel occurred in the service trains, the VHCF behavior of the pearlitic steels is rarely reported. A systematic experimental investigation on the VHCF behavior of the wheel steel should be investigated to illuminate the mechanism responsible for shattered rims and support the fatigue design of railway wheels.

The new research topic of VHCF has been explored in steels [6–7], titanium alloys [8–11] and aluminum alloys [12,13]. Two typical kinds of VHCF behavior have been defined: crack initiation from defect-free (Type I) and defect (Type II) sites [14,15]. In this study, the defects are related to inclusions or pores. When high-strength steels are subjected to VHCF, cracks initiate from interior nonmetallic inclusions, and the fatigue life is greater than 10^7 cycles. The whole region of crack initiation and early propagation exhibits a fish-eye (FiE) pattern, and the morphology around the inclusion is often relatively rough [16–20]. Moreover, nanograins (NGs) form in the fine granular area (FGA) after

cracks initiate under VHCF.

Pearlitic steel combines good wear and fatigue properties and is widely applied in different components of railway systems, including wheels, rails and axles. As known, these components are designed to bear millions of service miles with a fatigue life more than 10^7 cycles. Martensite [6–7,20], Austenite [21,22], Troostite [23] and Bainite [24,25] steels exhibit Type II VHCF. The engineering practice raises an urgent issue: does the pearlitic steel present the VHCF behavior?

In this paper, a systematic experimental investigation on the VHCF behavior of pearlitic steel extracted from railway wheels was conducted. First, samples of the pearlitic steel were subjected to rotating bending fatigue tests and ultrasonic fatigue tests, from which relevant $S-N$ curves were obtained. The fracture surfaces were observed by scanning electron microscopy (SEM), and crack initiation from interior inclusion was presented for the specimens of ultrasonic fatigue tests. The effects of inclusion size and stress ratio on the VHCF were evaluated. Finally, focused ion beam (FIB) microscopy and transmission electron microscopy (TEM) analyses were performed to characterize the microstructure of the fracture surface. A thin NG layer formed on the whole fracture surface.

* Corresponding author.

E-mail address: liuxiaolong@bjtu.edu.cn (X. Liu).

<https://doi.org/10.1016/j.ijfatigue.2020.105958>

Received 11 May 2020; Received in revised form 17 August 2020; Accepted 15 September 2020

Available online 21 September 2020

0142-1123/ © 2020 Elsevier Ltd. All rights reserved.

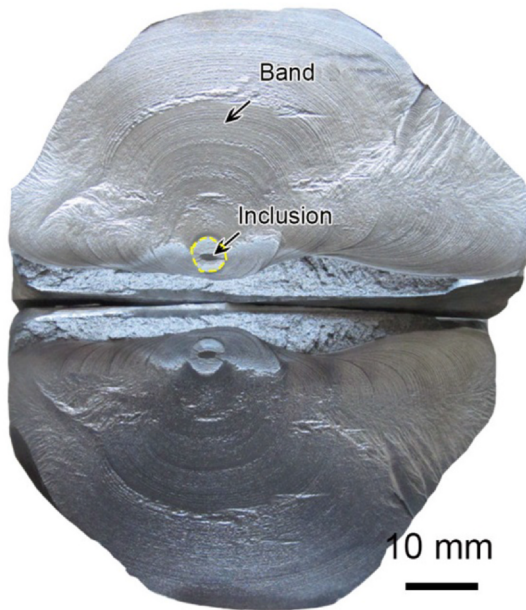


Fig. 1. Fracture surfaces of shattered rims [4].

2. Material and experimental procedures

2.1. Test material

The material used in this paper is a medium-carbon steel (CL60), which is a typical wheel steel in China. The chemical composition (mass percentage) of this material is 0.63C, 0.27Si, 0.72 Mn, 0.012P, 0.002 S, 0.12 Cr, 0.25 Cu and balance Fe. Fig. 2 shows the microstructure of CL60, which consists of pearlite (dark region) and ferrite (white region). The formation of pro-eutectoid ferrite is attributed to the heat treatment and carbon content. Pro-eutectoid ferrite is softer than pearlite, which plays the role of a crack initiation site in low-cycle fatigue and high-cycle fatigue. The mechanical properties of the material were determined by subjecting cylindrical specimens (diameter = 6 mm) to tension tests at a strain rate of 10^{-4} s^{-1} on an MTS 810 system. According to the results from three test specimens, the material had a yield strength of 560 MPa, a tensile strength of 906 MPa and a uniform elongation of 9.4%.

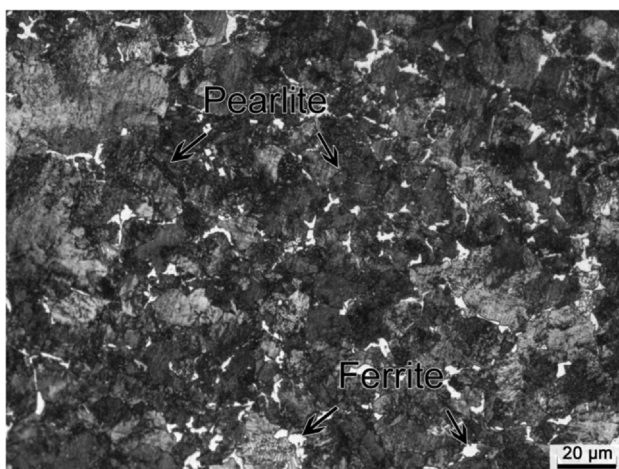


Fig. 2. Optical micrograph of the pearlitic steel microstructure.

2.2. Fatigue testing methods

Conventional fatigue testing was performed at room temperature in air by using a four-axis cantilever-type rotating bending machine, which was operated at 3150 rpm (52.5 Hz); the stress ratio in these tests was $R = -1$. Ultrasonic fatigue testing was conducted on an ultrasonic fatigue testing machine at a resonance frequency of 20 kHz at room temperature in air. The ultrasonic fatigue testing machine was installed on a conventional tensile machine (capacity 20 kN), which enabled ultrasonic cycling under a certain mean stress; the stress ratios in these tests were $R = -1$ and 0.3. Compressed air was used to cool the specimen during ultrasonic fatigue testing. Fig. 3a shows the sampling position of the fatigue test material, which is 15 mm underneath the wheel tread. After extraction, the material was processed into fatigue test specimens. Fig. 3b and c show the final shape and dimensions of the specimens used for rotating bending fatigue tests and ultrasonic fatigue tests, respectively. Note that the minimum diameter was 3.5 mm for both types of fatigue test samples. All fracture surfaces in this study were observed using an FEI Quanta 200 FEG field-emission type scanning electron microscope operated at a voltage of 20 kV, whereas the inclusions were analyzed by energy-dispersive spectroscopy (EDS). The TEM samples were prepared in the chamber of an FIB/SEM dual-beam system (FEI Helios Nanolab 600i). The TEM observations were conducted with an FEI Tecnai G2 F30 S-Twin transmission electron microscope. The selected area diffraction (SAD) pattern is 200 nm in diameter. An ASPEx Explorer SEM/EDS (FEI Company, Delmont, PA) automatic inclusion analysis system (acceleration voltage = 20 kV) was used to determine the composition, size, number, and distribution of inclusions present in the wheel steel samples (area = 50 mm^2).

3. Results

3.1. S-N curves

Fig. 4 shows the S-N curves for the three groups of specimens subjected to rotating bending fatigue tests and ultrasonic fatigue tests. The S-N curve under rotating bending loading (Fig. 4a) exhibits a horizontal asymptote shape with a clear fatigue limit, and surface crack initiation is observed only when the fatigue life is less than 10^6 cycles. The S-N curve under ultrasonic axial loading (Fig. 4b) exhibits a continuously descending shape, and the fatigue limit disappears at a fatigue life of 10^7 cycles, which is different from the typical stepwise S-N curves or duplex curves reported in high-strength steels [17,20]. Surface crack initiation was observed when the fatigue life was between 10^4 and 10^7 cycles, whereas interior crack initiation was observed when the fatigue life was between 10^6 and 10^9 cycles. The fatigue strength of the specimens at $R = -1$ under ultrasonic loading was approximately 250 MPa, which was markedly lower than that under conventional rotating bending loading (375 MPa). The occurrence of VHCF under axial loading is believed to reduce the fatigue strength. Moreover, the effect of the loading frequency on the fatigue behavior should be considered. The generation of heat in the specimen during ultrasonic fatigue testing at 20 kHz will also reduce the fatigue strength [23].

3.2. Fractography and dimensions of the inclusions and FIE region

Fig. 5 shows typical fracture surfaces of the specimens subjected to rotating bending loading. Note that all specimens failed as a result of surface cracks, wherein the surface cracks initiated at a single site (Fig. 5a) in seven of the 21 failed specimens and at multiple sites (Fig. 5b) in the remaining 14 specimens. No inclusions or defects were observed at the crack initiation sites. The corresponding fatigue lives of all specimens were less than 10^7 cycles.

Figs. 6 and 7 show fracture surfaces of the specimens subjected to ultrasonic axial loading at $R = -1$ and 0.3. When the fatigue life was less than 10^7 cycles, the cracks initiated from the surface, as shown in

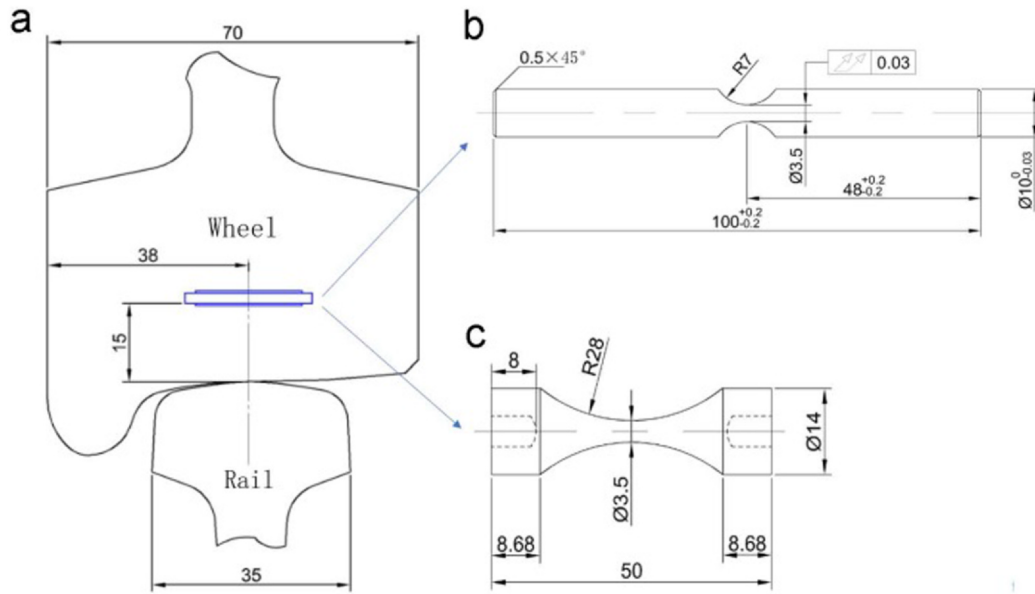


Fig. 3. (a) Test specimen sampling locations and specimen dimensions (units: mm) for the (b) rotating bending fatigue tests and (c) ultrasonic fatigue tests.

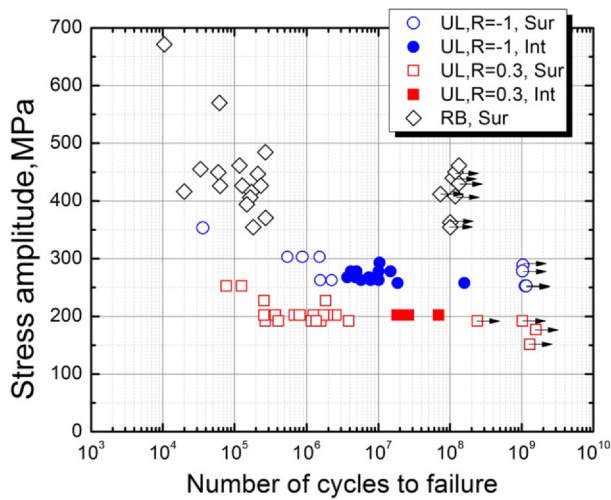


Fig. 4. *S-N* curves of CL60 under rotating bending loading and ultrasonic axial loading, RB: rotating bending loading, UL: ultrasonic axial loading, symbols with arrow: run out, hollow: surface crack initiation, solid: interior crack initiation.

Fig. 6a and 7a, and inclusions were observed at the crack initiation site (Fig. 6b and 7b). For the cases of interior crack initiation, the typical patterns of the fracture surfaces in ultrasonic fatigue test samples are shown in Fig. 6c and 7c. The whole region of crack initiation and early propagation exhibits an FiE pattern, and inclusions were found inside the FiE region; however, the FGA often reported for high-strength steel [24] was not very clear. As shown in Fig. 6d and 7d, the inclusions were irregular in shape and formed a sort of cluster. Fig. 7e presents the EDS results of the inclusions in the crack initiation region, and the location for the EDS analysis is marked by rectangle in Fig. 6d. The inclusion is MnS.

Fig. 8a and b presents high-magnification SEM images of the crack initiation region corresponding to Fig. 6d and 7d, respectively. For the case of crack initiation at $R = -1$, the fine grainy morphology (marked by arrows) that is similar to the reported FGA [6,7] were found around the inclusions, whereas intergranular and transgranular fractures (marked by arrows) were found near the inclusions when $R = 0.3$. Therefore, we can infer that the FGA formed only in the crack initiation region of the pearlitic steel during VHCF at $R = -1$. The microstructural change in the crack initiation region will be characterized hereinafter.

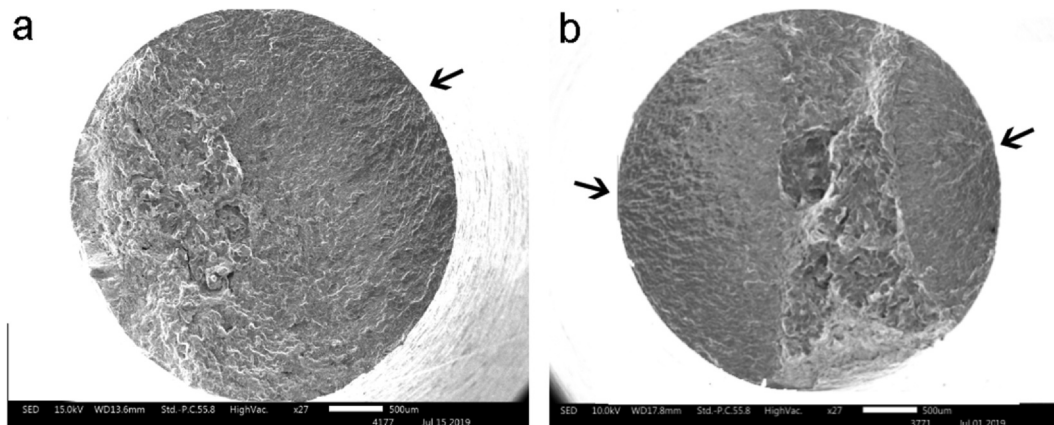


Fig. 5. Fracture surfaces of specimens subjected to rotating bending loading at $R = -1$: (a) single-site surface crack initiation ($\sigma_a = 446$ MPa and $N_f = 2.12 \times 10^5$ cycles) and (b) multisite surface crack initiation ($\sigma_a = 406$ MPa and $N_f = 1.66 \times 10^5$ cycles).

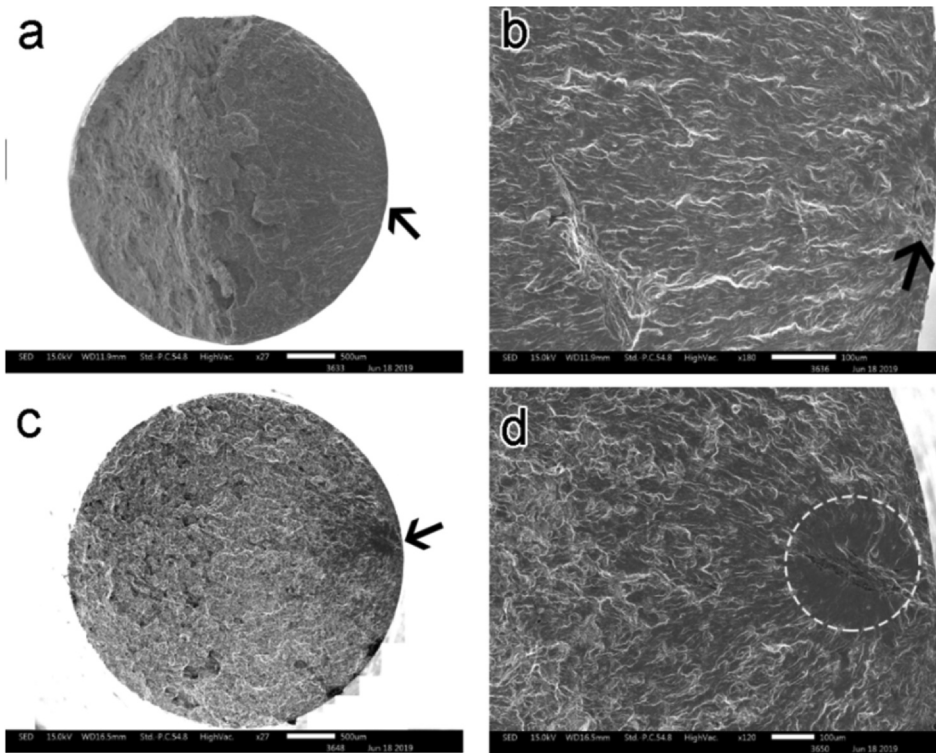


Fig. 6. Typical examples of fracture surfaces for specimens subjected to ultrasonic axial loading at $R = -1$. Surface crack initiation ($\sigma_a = 354$ MPa and $N_f = 3.6 \times 10^4$ cycles) at (a) low magnification and (b) high magnification. Interior crack initiation ($\sigma_a = 278$ MPa and $N_f = 1.0 \times 10^7$ cycles) at (c) low magnification and (d) high magnification.

3.3. Inclusions in the pearlitic steel

The types of inclusions observed by optical microscopy were mainly string-type MnS inclusions and near-globular Al_2O_3 inclusions, as shown in Fig. 9a. The Al_2O_3 inclusions were isolated, whereas the MnS inclusions formed clusters. The size and shape of the inclusions are the main parameters that will influence the VHCF property. In Murakami's results [26], the inclusion size plays a key role in the VHCF property, while the inclusion or defect shape can be ignored. In general, the formation of Al_2O_3 inclusions is related to the treatment of calcium in the secondary refining of molten steel. A total of 1263 MnS inclusions and 709 Al_2O_3 inclusions were detected by an ASPEX Explore in a 50 mm^2 area in the CL60 wheel steel. Fig. 9b shows the size distribution for MnS and Al_2O_3 inclusions. The results showed that all Al_2O_3 inclusions were within the size of 1–50 μm , whereas a few MnS inclusions were larger than 50 μm . Table 1 shows the typical morphology and size of the MnS and Al_2O_3 inclusions. These findings confirmed that the MnS inclusions were irregularly shaped, whereas the Al_2O_3 inclusions were globular. The MnS inclusions were twice as large as the Al_2O_3 inclusions. MnS inclusions are common in pearlitic steel. MnS inclusions have good plasticity, which can play the role of the strengthening phase like the precipitation in the aluminum alloy. By adding an appropriate amount of composite MnS inclusions, the yield strength of the steel is increased [27]. With increasing yield strength, the low-cycle fatigue (LCF) and high-cycle fatigue (HCF) properties can be improved [28,29]. However, for VHCF, the fatigue strength is inversely proportional to the inclusion size. The MnS inclusions easily formed long strip inclusions in the final product; hence, the number and size of inclusions were heterogeneously distributed, which resulted in the formation of inclusion clusters. Interior crack initiation can be easily caused by a cluster of MnS inclusions for its large size, which is why this phenomenon occurs in CL60 wheel steel during VHCF. Therefore, for CL60 wheel steel, an appropriate addition of MnS may improve the LCF and HCF properties, while the heterogeneous distribution of the inclusion will increase the risk of VHCF failure. Fig. 10.

4. Discussion

4.1. Quantitative evaluation of inclusions caused crack initiation

For each specimen, the values of $(\text{area})^{1/2}$ were calculated for the sizes of the inclusion cluster and FiE region. These results were plotted as a function of the fatigue life, as shown in Fig. 11a and b. The size of the inclusions $(\text{area})_{\text{inc}}^{1/2}$ was within a range of 50–200 μm , whereas that of the FiE region was within a range of 160–1108 μm . The interior crack initiated from the inclusion cluster. It is worth noting that the $(\text{area})_{\text{inc}}^{1/2}$ is related to the area sum of the inclusions in the cluster. The FiE sizes for the specimens at $R = 0.3$ were larger than those at $R = -1$. No FiE region was observed in the two specimens loaded at $R = 0.3$. The inclusions that caused interior crack initiation for these two specimens were within 20 μm from the surface. The disappearance of the FiE was attributed to the larger FiE size for high stress ratio and insufficient space for the formation of FiE. The sizes of the inclusions and FiE region did not have an obvious correlation with the fatigue life. These findings agree with the results reported in the literature [10,17,23].

The range of the stress intensity factor (SIF) at the front of the inclusions and FiE region was calculated by using the following equation [26,30]: $\Delta K_{\text{ini}} = 0.5\Delta\sigma\sqrt{\pi\sqrt{\text{area}}_{\text{ini}}}$, where $\Delta\sigma$ is the entire stress range when $R \geq 0$ or the positive part of the stress range when $R < 0$. The results were plotted as a function of fatigue life, as shown in Fig. 11. The values of ΔK_{inc} decreased with increasing fatigue life. The values of ΔK_{inc} at $R = -1$ and 0.3 were both less than the crack propagation threshold (CPT) (7.7 $\text{MPa}\cdot\text{m}^{1/2}$ at $R = -1$ and 4.93 $\text{MPa}\cdot\text{m}^{1/2}$ at $R = 0.3$ by experiments), indicating that the crack initiation and early propagation of the VHCF exhibited a short crack behavior.

Sun et al. proposed a model to describe the effects of the stress ratio on the fatigue strength of high-strength steels [31,32]: $\sigma_R = CN^l a_0^m \left(\frac{1-R}{2}\right)^\alpha$, where σ_R is the stress amplitude at a stress ratio of R , N is the fatigue life, a_0 is the defect size, and C , l , m and α are material parameters. The inclusion in the VHCF of high-strength steel is Al_2O_3 inclusions with near-globular shape. Here, the model was applied to describe the effects of MnS inclusion cluster with string shape.

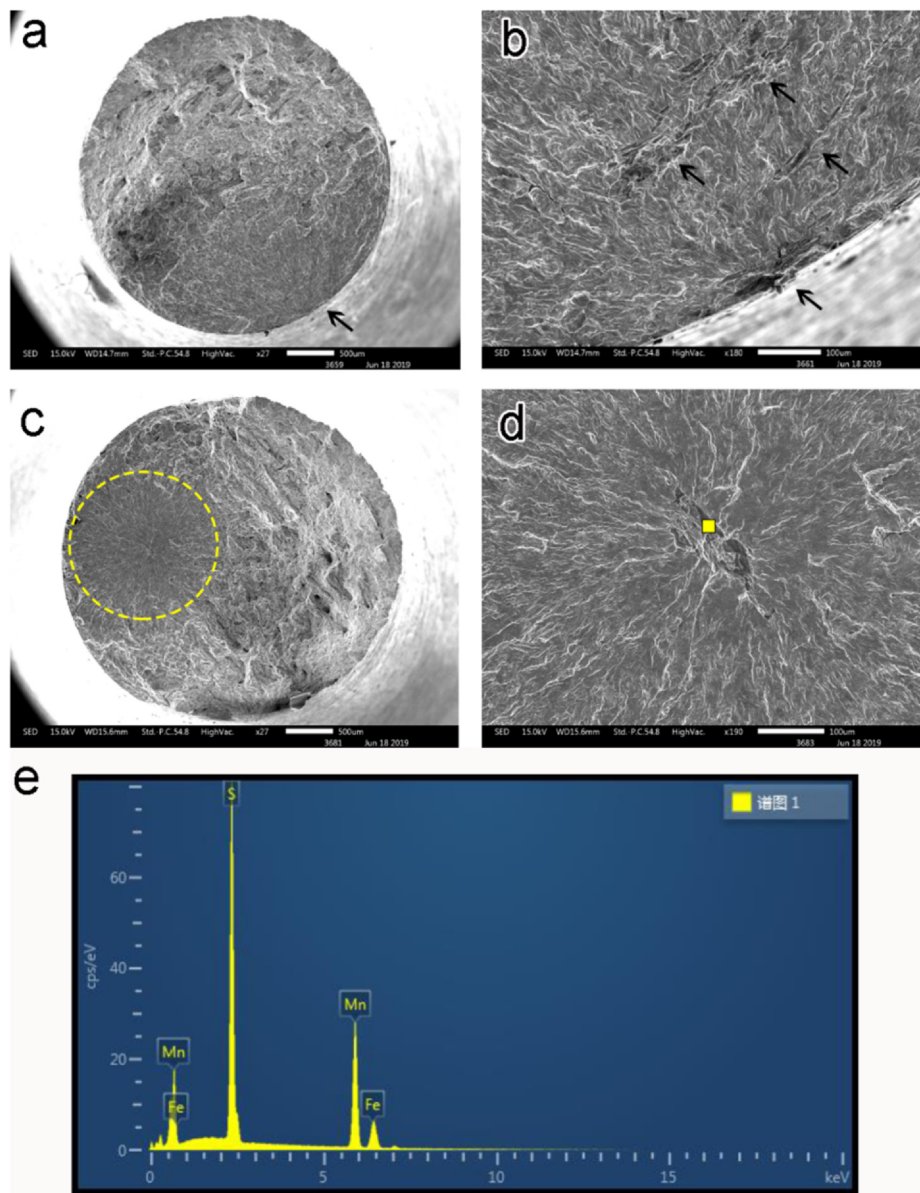


Fig. 7. Typical examples of fracture surfaces for specimens subjected to ultrasonic axial loading at $R = 0.3$. Surface crack initiation ($\sigma_a = 202$ MPa and $N_f = 2.6 \times 10^5$ cycles) at (a) low magnification and (b) high magnification. Interior crack initiation ($\sigma_a = 202$ MPa and $N_f = 1.8 \times 10^7$ cycles) at (c) low magnification and (d) high magnification. (e) EDS results of the inclusion in the crack initiation region.

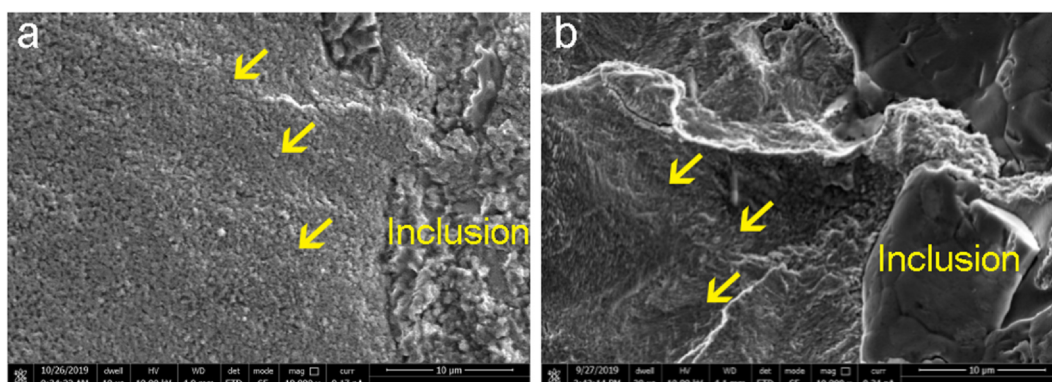


Fig. 8. High-magnification SEM images of the crack initiation region in the pearlitic steel during VHCF at (a) $R = -1$ and (b) $R = 0.3$.

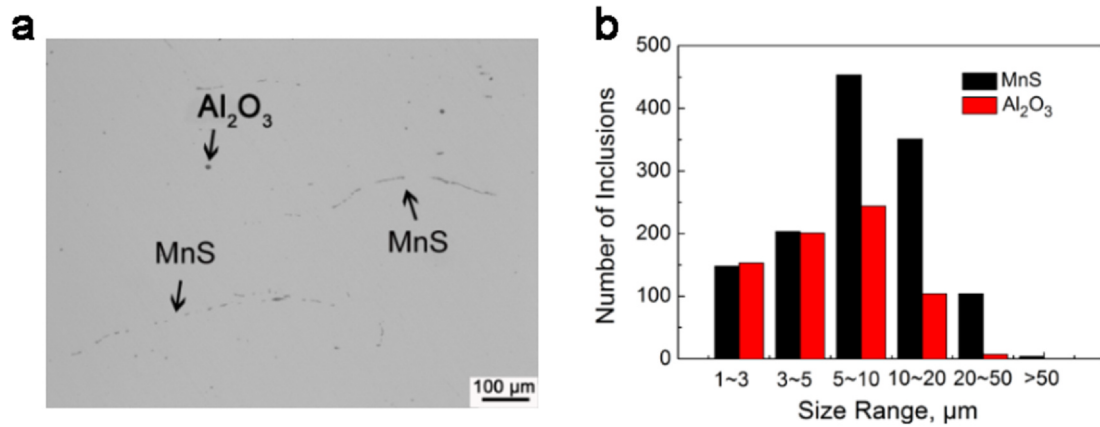
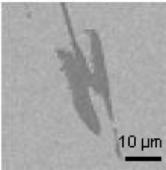
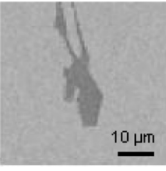
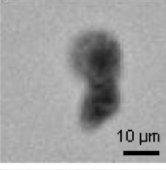
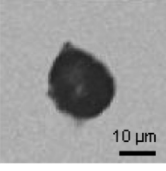


Fig. 9. (a) Typical morphology of MnS and Al₂O₃ inclusions in the wheel steel samples, (b) size distribution for MnS and Al₂O₃ inclusions in the wheel steel.

Table 1
Typical morphology and size of MnS and Al₂O₃ inclusions in the wheel steel samples.

Image	Inclusion type	D _{max} (µm)	D _{min} (µm)	Area (µm ²)
	MnS	38.3	11.0	436.8
	MnS	42.2	8.8	380.5
	Al ₂ O ₃	20.0	11.4	207.3
	Al ₂ O ₃	18.5	14.7	197.5

The equation was developed to estimate the relationship among the inclusion size, fatigue life and fatigue strength for specimens that failed from the interior inclusion based on experimental results. In this study, m was taken as $-1/6$. The material parameters C and l were determined by fitting the experimental data: $C = e^{6.7}$ and $l = -0.020$. The parameter α was taken as 0.29, which was determined by fitting the experimental data from the samples subjected to VHCF at $R = 0.3$. For low-cycle and high-cycle fatigue, the Goodman formula and Gerber formula are usually used to correlate stress ratio and fatigue strength. Here, this model with the obtained parameters can be applied to correlate the stress ratio and fatigue strength in the VHCF behavior of the pearlitic steel.

The effects of inclusion size on the VHCF also can be evaluated by the model. The fatigue data at $R = 0.3$ were amended by the model to eliminate the effects of stress ratio, and then the fatigue strength that varies with inclusion size was investigated. Fig. 12 shows the fatigue

strength obtained by the model and the experimental data for the pearlitic steel. The maximum inclusion size of the specimens was 171 µm, whereas the minimum inclusion size was 44.5 µm. The fatigue strength obtained by the model using the minimum and maximum inclusion sizes are represented by red and black lines, respectively. The former is generally higher than the experimental results and therefore can be regarded as the upper bound of the experimental fatigue strength results. The latter is generally smaller than the experimental results and therefore can be regarded as the lower bound of the experimental fatigue strength results. The fatigue strength obtained by the model using the average inclusion size, which is represented by a blue line, is in the middle of the range of the experimental results. Hence, the corresponding S-N curve seems to be moderate. This finding indicates that the fatigue life model can describe the relationship among the fatigue strength, fatigue life, defect size, and stress ratio for pearlitic steel subjected to VHCF.

Inclusion size, shape and position may influence the VHCF property of the steel. In general, the inclusion size is a crucial geometrical factor compared with the factors of inclusion shape and position. The specimens fractured from the angular shape of inclusion tends to show slightly shorter fatigue lives compared with those fractured from spherical inclusion [33,34]. In this paper, all the interior cracks initiated from the angular shape of MnS inclusion instead of near-globular Al₂O₃ inclusions, indicating that angular shape promoted the interior crack initiation. Fig. 13 presents relationship between inclusion depth and fatigue life. Most of the interior crack initiation size located at not more than 200 µm away from the surface. The depth of inclusion does not affect the fatigue life obviously. This is in agreement with the results in the literature [23,26].

4.2. Microstructure characterizations for the cases at $R = -1$ and 0.3

The fracture surface of a specimen that failed at $\sigma_a = 202$ MPa, $N_f = 1.8 \times 10^7$ cycles, and $R = 0.3$, as shown in Fig. 7c and d, was selected for analyzing the mechanisms of microstructural changes at a positive stress ratio. Two areas in the FiE region were chosen: Region A, which was near the inclusion, and Region B, which was far away from the inclusion (Fig. 14a and b). An FIB was used to mill these two regions into thin films for TEM observation (Fig. 14c and d); the films milled from Region A and Region B had thicknesses of 65 nm and 80 nm and cross-sectional dimensions of 5.0×4.0 µm² and 4.8×4.1 µm², respectively.

A detailed TEM morphology of the thin film from Region A is shown in Fig. 15a, indicating the original pearlitic microstructure. Furthermore, the SAD patterns at three selected points, P1 and P2 underneath the fracture surface and P3 far away from the fracture surface, are shown in Fig. 15b, c and d, respectively. Note that P1, P2 and P3 are ferrite within the pearlite. The SAD patterns of points P1, P2 and P3

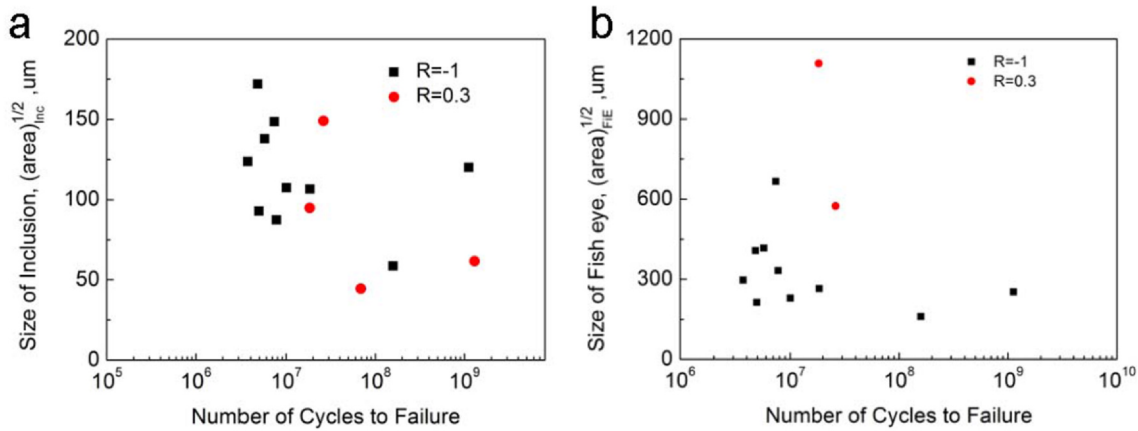


Fig. 10. Size of the (a) inclusions and (b) FiE region for the fracture surfaces generated by loading at $R = 0.1$ and 0.3 .

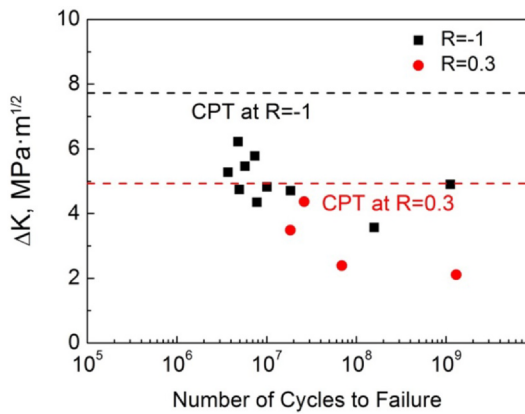


Fig. 11. Relationships between the SIF range and fatigue life.

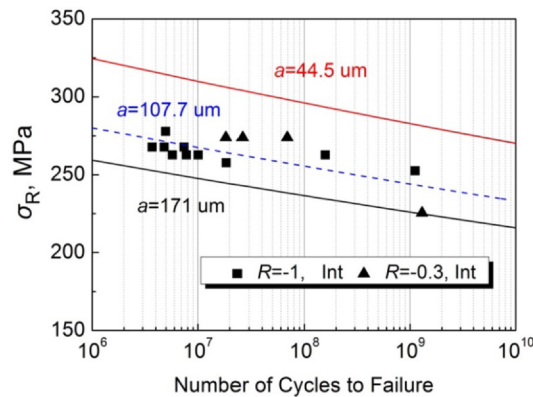


Fig. 12. Comparison of fatigue strength obtained by the model and the experimental data. Note that the model results obtained using the maximum, minimum, and average inclusion size from the experimental data are represented by the black line, red line, and blue line, respectively.

have isolated spots implying normal diffraction of a single grain, which is the typical body-centered cubic (BCC) structure. The SAD patterns indicate the microstructure only at local locations. Fig. 15e and f shows a high-magnification bright-field image (BFI) and corresponding dark-field image (DFI) around P2, which reveals a more distinct morphology of the microstructure in the crack initiation region. The microstructure has the features of pearlite. Therefore, we can infer that no microstructural changes occurred in the crack initiation site for the samples subjected to VHCF at a positive stress ratio ($R = 0.3$).

We now examine the microstructure of Region B in the FiE region of

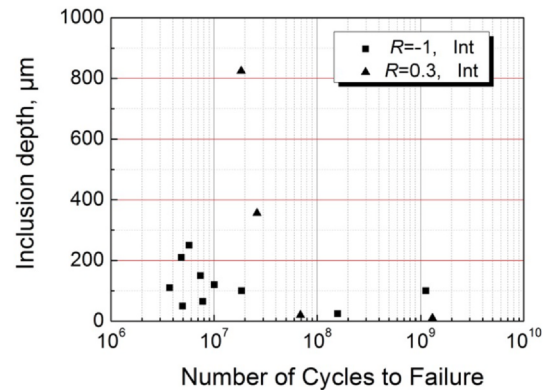


Fig. 13. Relationship between inclusion depth and fatigue life.

the pearlitic steel samples subjected to VHCF at $R = 0.3$ (Fig. 16). The original pearlite can be observed in the BFI, indicating that grain refinement does not occur in the FiE region. The SAD patterns of P4, P5 and P6 underneath the fracture surface are isolated spots with a single grain, which confirms that no microstructure changes occurred in the FiE region.

The fracture surface of a specimen that failed at $\sigma_a = 278$ MPa, $N_f = 1.0 \times 10^7$ cycles, and $R = -1$, as shown in Fig. 6d, was selected for analyzing the mechanisms of microstructure changes at a negative stress ratio. Two regions were chosen for this analysis: Region C, which was near the inclusion, and Region D, which was far away from the inclusion (Fig. 17a). An FIB was used to mill these two regions into thin films for TEM observation (Fig. 17b and c); the film milled from Region C and Region D had thicknesses of 49 nm and 51 nm and cross-sectional dimensions of $4.9 \times 4.0 \mu m^2$ and $5.0 \times 4.0 \mu m^2$, respectively.

An overall view of the thin film milled from Region C, as shown in Fig. 18a, has different features than the film obtained at $R = 0.3$ (Fig. 15a). An NG layer, which is marked by the dashed line, overlays the pearlite that formed during fatigue cycling. Points P-A, P-B and P-C in the NG layer are selected to conduct SAD analysis. The SAD patterns of these three points are discontinuous diffraction circles, implying a number of grains within the 200 nm diffraction area. Furthermore, DFIs were taken near these three points, as shown in Fig. 18a, b and c, which confirmed that NGs formed in the crack initiation region for the samples subjected to VHCF at $R = -1$. The dimensions of these NGs are within 10 nm in width and 100 nm in length. The formation of NGs in the crack initiation region has also been reported in high-strength steel and titanium alloys subjected to VHCF.

Fig. 19a shows a TEM image of Region D (Fig. 16a), illustrating the profile of the fracture surface for the microstructure underneath the FiE region, which also contains three layers: a Pt layer, an NG layer of

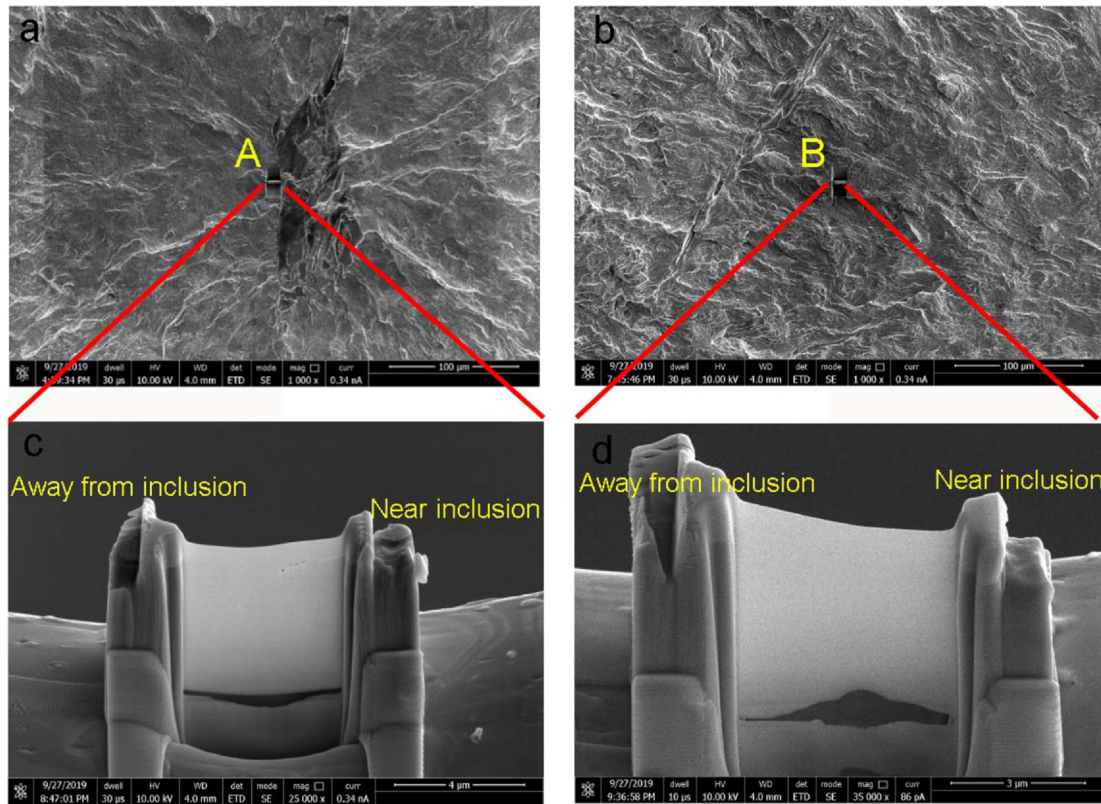


Fig. 14. SEM images of the specimen surface ($\sigma_a = 202$ MPa, $N_f = 1.8 \times 10^7$ cycles, and $R = 0.3$): the locations of (a) Region A and (b) Region B milled by FIB and an overall view of the thin film samples from (c) Region A and (d) Region B.

microstructure underneath the fracture surface, and the original pearlite with a clear grain boundary. Three points (P-D, P-E and P-F) in the NG layer were selected for SAD analysis, which confirmed the formation of NGs. Fig. 19b, c and d shows high-magnification DFIs taken near P-D, P-E and P-F, which reveal clear NGs with sizes in the tens of nanometers at the surface. The formation of NGs in the FiE region is rarely reported and is likely caused by the cyclic compression of the crack surface during fatigue cycling.

FIB enables not only the preparation of large, uniformly thick, site

specific samples, but also the fabrication of lamellae used for TEM samples from composite samples consisting of inorganic and organic materials with very different properties. The application of FIB to prepare samples for TEM investigation was very popular. However, the effect of the FIB fabrication on the variation of grain structure should be ruled out. In general, FIB can induce damage, Ga contamination [35] and austenite transformation [36]. FIB inducing the nanograins formation has not been reported. Meanwhile, if the FIB can induce nanograins on the surface of the TEM samples, nanograins should be

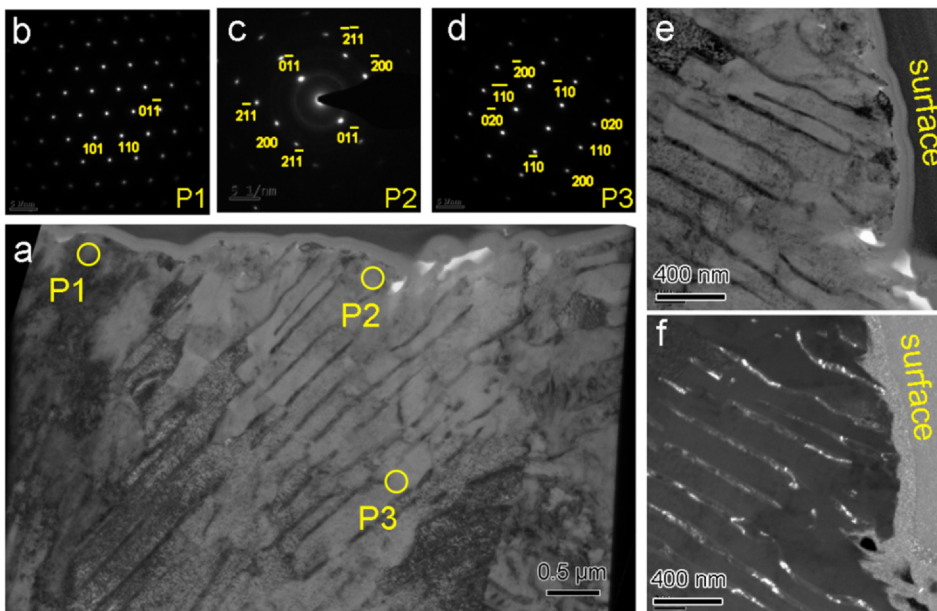


Fig. 15. TEM images, SAD patterns, and a high-magnification BFI and DFI of the crack initiation region for the pearlitic steel samples subjected to VHCF at a positive stress ratio: (a) TEM image of Region A, (b) SAD pattern of P1 (underneath the fracture surface), (c) SAD pattern of P2 (underneath the fracture surface), (d) SAD pattern of P3 (far away from the fracture surface), and a (e) BFI and (f) DFI of the microstructure features around P2.

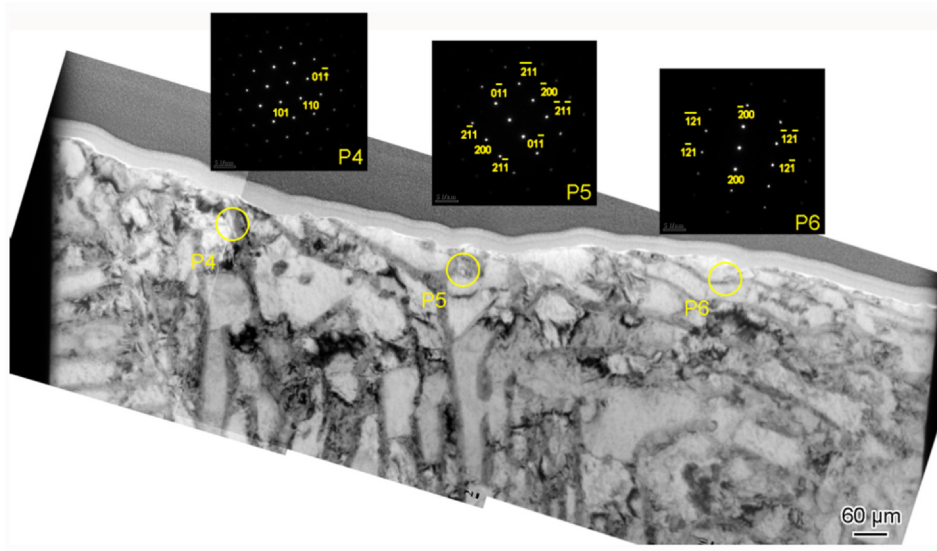


Fig. 16. BFI and associated SAD patterns of the FiE region in the pearlitic steel samples subjected to VHCF at a positive stress ratio.

observed on both TEM samples at $R = -1$ and 0.3 which is conflicted with the experimental results. Therefore, it is believed that the nanograins formed during the fatigue experiments.

In summary, the nanograins formed at a negative stress ratio and disappeared at a positive stress ratio. The difference between the negative and positive stress ratios is that a cyclic compressive stress exists in the negative stress ratio. The compressive stress will cause contact between the early crack surfaces. However, the compressive stress is within 300 MPa, which is less than the yield strength of 560 MPa. In general, severe plastic deformation can refine the grains to nanograins

[37,38]. Nanograins also formed in the friction pair such as brake disc and pad [39], wheel and rail [40]. At the beginning of the interior crack initiation, the crack is Mode II crack determined by the shear stress. The relative displacement between the two crack surfaces causes the grain refinement.

5. Conclusions

This paper investigated the effects of inclusion size and stress ratio on the VHCF behavior of pearlitic steel. The following conclusions can

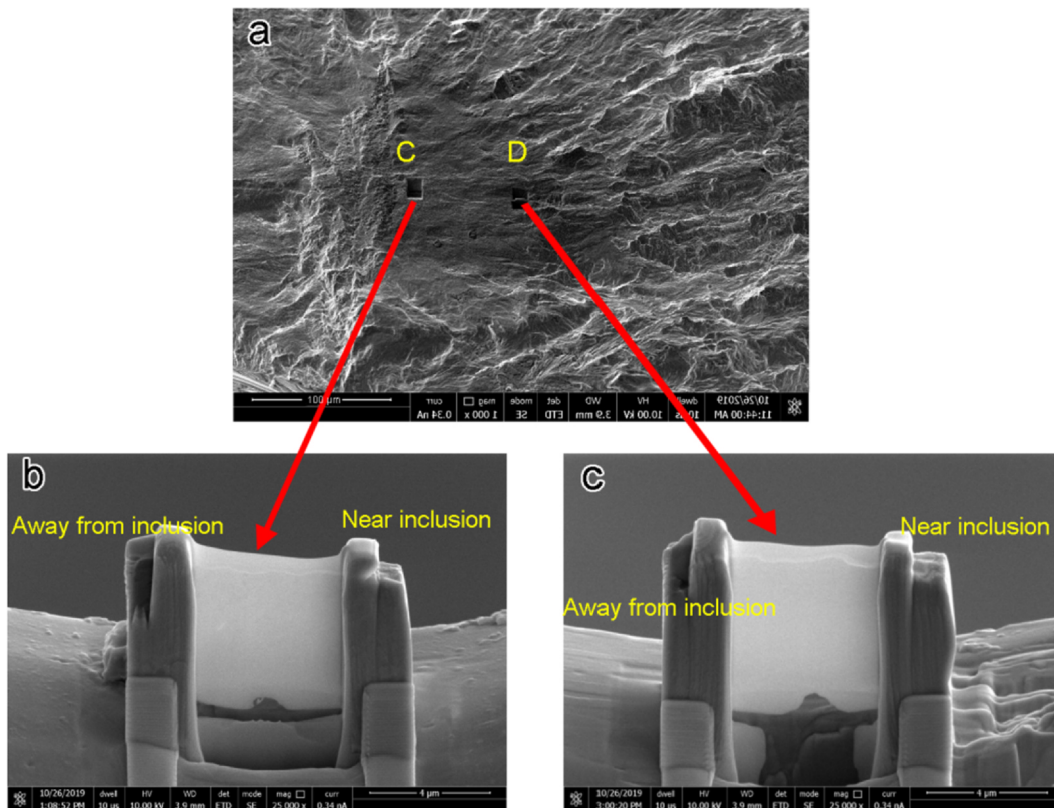


Fig. 17. SEM images of the specimen surface ($\sigma_a = 278$ MPa and $N_f = 1.0 \times 10^7$ cycles): (a) the location of Region C and Region D milled by FIB and an overall view of the thin film samples from (b) Region C and (c) Region D.

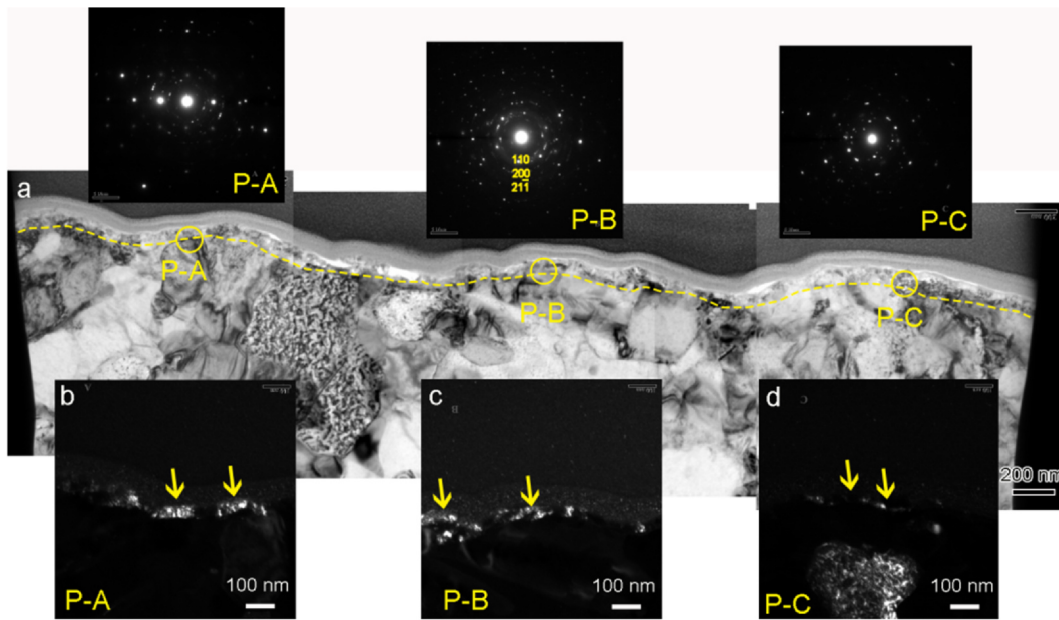


Fig. 18. (a) TEM images of Region C (near the inclusion), which show an overview of the substructures below the fracture surface and the corresponding SAD patterns of P-A, P-B and P-C. High-magnification DFIs taken near (b) P-A, (c) P-B and (d) P-C.

be drawn from this study.

- (1) The $S-N$ curve under rotating bending loading exhibited a horizontal asymptote shape and a clear fatigue limit. In contrast, the $S-N$ curve under ultrasonic axial loading exhibited a continuously descending shape, and the fatigue limit disappeared at a fatigue life of 10^7 cycles. The fatigue strength at $R = -1$ under ultrasonic loading decreased to approximately 250 MPa, which was markedly lower than that under conventional rotating bending loading (375 MPa).
- (2) Only surface crack initiation occurred in the fracture surfaces under

rotating bending loading, whereas both surface and interior crack initiation occurred for the cases under ultrasonic axial loading. The interior cracks initiated from the MnS inclusions. An FGA formed in the crack initiation region only for the samples subjected to VHCF at $R = -1$.

- (3) MnS and Al_2O_3 inclusions were detected in the pearlitic steel. All instances of interior crack initiation were caused by the MnS inclusions since the MnS inclusions were larger than the Al_2O_3 inclusions. A fatigue model was used to evaluate the effects of the stress ratio and inclusion size on the fatigue strength, and the results from the model were in good agreement with the experimental

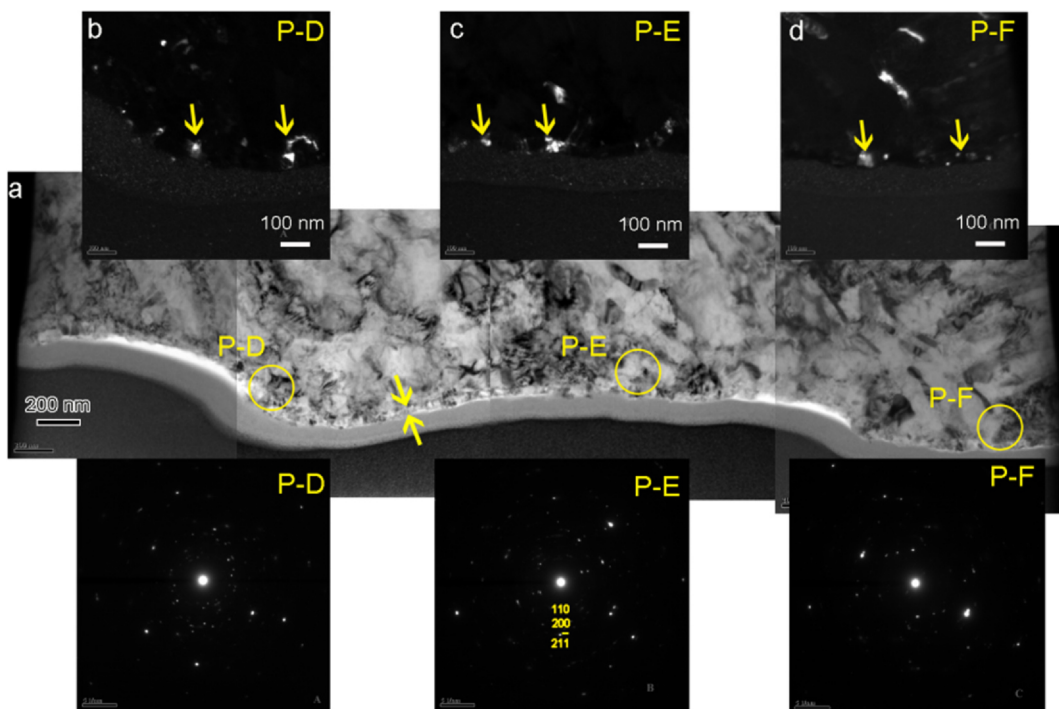


Fig. 19. (a) TEM images of Region D (far away from the inclusion and in the FiE region), which show an overview of the substructures below the fracture surface and the corresponding SAD patterns of P-D, P-E and P-F, high-magnification DFIs taken near (b) P-D, (c) P-E and (d) P-F.

results.

- (4) NGs formed in the crack initiation region and the FiE region of the samples subjected to VHCF at $R = -1$; this phenomenon was attributed to the cyclic compression between the crack surfaces during fatigue cycling.

Declaration of Competing Interest

The authors (Tao Cong, Guian Qian, Guanzhen Zhang, Si Wu, Xiangnan Pan, Leiming Du, Xiaolong Liu) declared that they have no conflicts of interest to this work. We declare that we do not have any commercial or associative interest that represents a conflict of interest in connection with the work submitted.

Acknowledgments

The authors would like to acknowledge financial support from the National Natural Science Foundation of China (No. 11802011), the National Key Research and Development Program of China (No. 2017YFB0702004), the Development Project of China Railway (No. J2019J004) and the China Academy of Railway Sciences Corporation Limited (No. 2019YJ097).

References

- Ekberg A, Kabo E, Nielsen JCO, Lundén R. Subsurface initiated rolling contact fatigue of railway wheels as generated by rail corrugation. *Int J Solids Struct* 2007;44:7975–87.
- Liu Y, Liu L, Mahadevan S. Analysis of subsurface crack propagation under rolling contact loading in railroad wheels using FEM. *Eng Fract Mech* 2007;74:2659–74.
- Ekberg A, Akesson B, Kabo E. Wheel/rail rolling contact fatigue – Probe, predict, prevent. *Wear* 2014;314:2–12.
- Cong Tao, Han Jianmin, Hong Youshi, Domblesky Joseph, Liu Xiaolong. Shattered rim and shelling of high-speed railway wheels in the very-high-cycle fatigue regime under rolling contact loading. *Eng Fail Anal* 2019;97:556–67.
- Zhang Guanzhen, Ren Ruiming. Study on typical failure forms and causes of high-speed railway wheels. *Eng Fail Anal* 2019;105:1287–95.
- Sakai T, Sato Y, Oguma N. Characteristic S-N properties of high-carbon-chromium-bearing steel under axial loading in long-life fatigue. *Fatigue Fract Eng Mater Struct* 2002;25:765–73.
- Shiozawa K, Lu L, Ishihara S. S-N curve characteristics and subsurface crack initiation behaviour in ultra-long life fatigue of a high carbon-chromium bearing steel. *Fatigue Fract Eng Mater Struct* 2001;24:781–90.
- Qian Guian, Jian Zhibo, Pan Xiangnan, Berto Filippo. In-situ investigation on fatigue behaviors of Ti-6Al-4V manufactured by selective laser melting. *Int J Fatigue* 2020;133:1–9.
- Qian Guian, Yanfeng Li DS, Paolino A, Tridello F Berto, Youshi Hong. Very-high-cycle fatigue behavior of Ti-6Al-4V manufactured by selective laser melting: Effect of build orientation. *Int J Fatigue* 2020;136:105628.
- Liu Xiaolong, Chen Erqing, Zeng Fan, Cong Tao, Domblesky Joseph P. Mechanisms of interior crack initiation in very-high-cycle fatigue of high-strength alloys. *Eng Fract Mech* 2019;212:153–63.
- Liu Xiaolong, Sun Chengqi, Hong Youshi. Faceted crack initiation characteristics for high-cycle and very-high-cycle fatigue of a titanium alloy under different stress ratios. *Int J Fatigue* 2016;92:434–41.
- Wang QY, Lib T, Zenga XG. Gigacycle fatigue behavior of high strength aluminum alloys. *Procedia Eng* 2010;2:65–70.
- Brugger Charles, Palin-Luc Thierry, Osmond Pierre, Blanc Michel. Gigacycle fatigue behavior of a cast aluminum alloy under biaxial bending: experiments with a new piezoelectric fatigue testing device. *Procedia Struct Integrity* 2016;2:1173–80.
- Li SX. Effects of inclusions on very high cycle fatigue properties of high strength steels. *Int Mater Rev* 2012;57:92–114.
- Zimmermann M. Diversity of damage evolution during cyclic loading at very high numbers of cycles. *Int Mater Rev* 2012;57:73–91.
- Huang Zhi Yong, Wagner Danièle, Bathias Claude, Paris Paul C. Subsurface crack initiation and propagation mechanism in the gigacycle fatigue. *Acta Mater* 2010;58:6046–54.
- Li W, Deng H, Sun Z, Zhang Z, Lu L, Sakai T. Subsurface inclusion-induced crack nucleation and growth behaviors of high strength steels under very high cycle fatigue: Characterization and microstructure-based modeling. *Mater Sci Eng, A* 2015;641:10–20.
- Sander M, Muller T, Lebahn J. Influence of mean stress and variable amplitude loading on the fatigue behaviour of a high-strength steel in VHCF regime. *Int J Fatigue* 2014;62:10–20.
- Zhu MingLiang, Jin Long, Xuan FuZhen. Fatigue life and mechanistic modeling of interior micro-defect induced cracking in high cycle and very high cycle regimes. *Acta Mater* 2018;157:259–75.
- Hong Y, Liu X, Lei Z, Sun C. The formation mechanism of characteristic region at crack initiation for very-high-cycle fatigue of high-strength steels. *Int J Fatigue* 2016;89:108–18.
- Grigorescu AC, Hilgendorff PM, Zimmermann M, Fritzen CP, Christ HJ. Cyclic deformation behavior of austenitic Cr–Ni-steels in the VHCF regime: Part I - Experimental study. *Int J Fatigue* 2016;93:250–60.
- Hilgendorff PM, Grigorescu Andrei Cristian, Zimmermann M, Fritzen CP, Christ HJ. Cyclic deformation behavior of austenitic Cr–Ni-steels in the VHCF regime: Part II – Microstructure-sensitive simulation. *Int J Fatigue* 2016;93:261–71.
- Zhao A, Xie J, Sun C, Lei Z, Hong Y. Effects of strength level and loading frequency on very-high-cycle fatigue behavior for a bearing steel. *Int J Fatigue* 2012;38:46–56.
- Gao Guhui, Zhang Baoxiang, Cheng Cheng, Zhao Ping, Zhang Han, Bai Bingzhe. Very high cycle fatigue behaviors of bainite/martensite multiphase steel treated by quenching partitioning tempering process. *Int J Fatigue* 2016;92:203–10.
- Gao Guhui, Liu Rong, Wang Kun, Xiaolu Gui RDK, Misra Bingzhe Bai. Role of retained austenite with different morphologies on sub-surface fatigue crack initiation in advanced bainitic steels. *Scr Mater* 2020;184:12–8.
- Murakami Y. *Metal Fatigue: Effects of Small Defects and Nonmetallic Inclusions*. London: Elsevier; 2002.
- Li Zhaodong, Zhou Shitong, Yang Caifu, Yong Qi-long. High/very high cycle fatigue behaviors of medium carbon pearlitic wheel steels and the effects of microstructure and non-metallic inclusions. *Mater Sci Eng, A* 2019;764:138208.
- Yanmei Li, Fuxian Zhu, Fengping Cui, K. Fang. Analysis of Forming Mechanism of Lamination Defect of Steel Plate. *Journal of Northeastern University* 2007; 28: 1002-1005.
- Li Menglong, Wang Fuming, Li Changrong, Yang Zhanbing, Meng Qingyong, Tao Sufen. Effects of cooling rate and Ai on MnS formation in medium-carbon non-quenched and tempered steels. *Int J Miner Metall Mater* 2015;22:589–97.
- Murakami Y, Nomoto T, Ueda T. Factors influencing the mechanism of superlong fatigue failure in steels. *Fatigue Fract Eng Mater Struct* 1999;22:581–90.
- Sun CQ, Lei ZQ, Xie JJ, Hong YS. Effects of inclusion size and stress ratio on fatigue strength for high-strength steels with fish-eye mode failure. *Int J Fatigue* 2013;48:19–27.
- Sun CQ, Liu XL, Hong YS. A two-parameter model to predict fatigue life of high-strength steels in a very high cycle fatigue regime. *Acta Mech Sinica* 2015;31:383–91.
- Y. Murakami, K. Kawakami, W.E. Duckworth. Quantitative evaluation of effects of shape and size of artificially introduced alumina particles on the fatigue strength of 1.5NiCrMo (En24) steel. *Int J Fatigue* 1991; 13: 489-499.
- Mayer J, Giannuzzi LA, Kamino T, Michael JR. TEM sample preparation and FIB-induced damage. *MRS Bull* 2007;32:400–7.
- Knipling KE, Rowenhorst DJ, Fonda RW, et al. Effects of focused ion beam milling on austenite stability in ferrous alloys. *Mater Charact* 2010;61(1):1–6.
- Duckworth WE, Ineson E. The effects of externally introduced alumina particles on the fatigue life of En24 steel. *Iron Steel Inst* 1963;77:87–103.
- Liu XL, Yuan FP, Zhu YT, Wu XL. Extraordinary Bauschinger effect in gradient structured copper. *Scr Mater* 2019;150:57–60.
- T.H. Fang, W.L. Li, N.R. Tao, K. Lu. Revealing extraordinary intrinsic tensile plasticity in gradient nano-grained copper. *Science* 2011; 331: 1587–1590.
- Wang Zhizhong, Han Jianmin, et al. Crack propagation and microstructural transformation on the friction surface of a high-speed railway brake disc. *Wear* 2019;428–429:45–54.
- Lojkowski W, Djahanbakhsh M, Biirklé G. Nanostructure formation on the surface of railway tracks. *Mater Sci Eng A* 2001;303:197–208.